Astronomical Techniques and Instruments, Vol. 3, May 2026, 235–249

Article **Open Access**

Sparse optimization and multi-performance enhancement of a high frequency to very high frequency wideband radio array using a genetic algorithm

Yifeng Qin[1], Jiarui Di[2], Liang Dong[2*], Zhang Ning[3], Yan Liu[4], Lesheng He[1], Abidin Zamri Zainal[5], Huanhuan Xie[6], Latef Abdul Tarik[5], Wei He[6], Othman Mohamadariff[5]

[1]*School of Information*, *Yunnan University*, *Kunming* 650500, *China*

[2]*Yunnan Observatories*, *Chinese Academy of Sciences*, *Kunming* 650011, *China*

[3]*Urumqi Monitoring Station of State Radio Monitoring Center*, *Urumqi* 830011, *China*

[4]*School of Physics and Electronic Information*, *Yunnan Normal University*, *Kunming* 650500, *China*

[5]*Department of Electrical Engineering*, *Universiti Malaya*, *Kuala Lumpur* 50603, *Malaysia*

[6]*Xi'an Research Institute of Navigation Technology*, *Xi'an* 710068, *China*

*Correspondence: dongliang@ynao.ac.cn

Received: September 8, 2025; Accepted: November 17, 2025; Published Online: November 18, 2025; https://doi.org/10.3724/ati2025077; https://cstr.cn/32083.14.ati2025077

Citation: Qin, Y. F., Di, J. R., Dong, L., et al. 2026. Sparse optimization and multi-performance enhancement of a high frequency to very high frequency wideband radio array using a genetic algorithm. *Astronomical Techniques and Instruments*, **3**(3): 235−249. https://doi.org/10.3724/ati2025077.

Abstract: The High Frequency (HF, 3–30 MHz) to Very High Frequency (VHF, 30–300 MHz) band is a critical observational window in radio astronomy, playing a key role in the study of early-universe reionization, space weather monitoring, and solar physics. We determine whether a genetic algorithm-optimized sparse configuration of a 64-element planar radio antenna array can minimize the peak sidelobe level and enhance performance within the 10–90 MHz frequency range, compared with a regular configuration. The sparse-optimized array achieves a 1.04 dB reduction in peak sidelobe level across the frequency band compared with the regular array. Sensitivity improves significantly at all frequency points, with increases of up to 56% at 10 MHz and 45% at 50 MHz. At 90 MHz, the sensitivity matches that of the regular array. At three representative frequencies (50 MHz, 60 MHz, and 70 MHz), grating lobe suppression tests at different scan angles show that the regular array shows prominent grating lobes at specific scan angles (θ = 53° at 50 MHz, θ = 30° at 60 MHz, and θ = 15° at 70 MHz). By contrast, the sparse array shows no observable grating lobes, confirming its superior suppression capability. At wide bandwidths, a sparse array optimized with a genetic algorithm outperforms a regular array in peak sidelobe level, sensitivity, and scanning range, supporting its use as a better technical solution for radio astronomical observations.

Keywords: HF-VHF band; Sparse array; Genetic algorithm; Peak side lobe level; Sensitivity

1. INTRODUCTION

The High Frequency (HF, 3–30 MHz) to Very High Frequency (VHF, 30–300 MHz) frequency range serves as a vital observational window in radio astronomy[1], offering significant research value in various domains such as space weather and solar physics studies[2,3], monitoring of planetary burst activities within the solar system[4], transient source detection[5], and investigations of reionization processes in the early universe[6]. However, due to the relatively long wavelengths in this frequency band, large-aperture reflector antennas face limitations that can prevent them from meeting observational requirements. Consequently, high-gain antenna arrays, synthesized from multiple radiating elements, have become the mainstream solution for observations in this frequency regime[7].

The spatial arrangement of antenna elements is a critical factor that determines the performance of an array system. Antenna arrays are generally categorized into two types: uniformly spaced arrays (regular arrays) and non-uniformly spaced arrays (sparse arrays). In wideband operational scenarios, to prevent grating lobes from appearing in the radiation pattern at the upper end of the frequency band, traditional regular arrays typically constrain the element spacing to within half a wavelength[8]. However, in practical engineering applications, physical constraints on the antenna structure and mutual coupling effects between elements often make it difficult to maintain such close spacing[9]. As a result, the strict requirement of grating-lobe-free performance at the upper operating frequency becomes challenging to meet the relation,

$$d_{\min} < \frac{\lambda_{\min}}{1+|\sin\theta_{\max}|}, \tag{1}$$

where θ is the scan angle in degrees, and $\lambda_{\min}$ is the shortest wavelength within the operational frequency band, which corresponds to the upper frequency boundary[9]. When the inter-element spacing, $d_{\min}$, is less than $\lambda_{\min}/2$, the radiation pattern at the highest frequency does not produce grating lobes. When d exceeds $\lambda_{\min}/2$, grating lobes emerge in the radiation pattern at the upper frequency, and their intensity increases with element spacing. These grating lobes may have amplitudes comparable to the main lobe, complicating the ability to discern between the main lobe and grating lobes. This phenomenon leads to a substantial reduction in sensitivity and signal-to-noise ratio (SNR) within the main beam. Sensitivity reflects the capability of a radio telescope's receiving system to detect weak signals[10], and serves as a critical performance metric for evaluating radio telescopes. To mitigate grating lobes, sparse arrays are commonly used. By disrupting the periodicity of the array factor, sparse arrays can suppress grating lobes effectively. With this advantage, the design and optimization of sparse arrays have become a key research area in antenna array technology[11].

Introducing sparse array technology into radio astronomy provides significant advantages. It enhances system interference resistance, improves detection sensitivity, and expands sky coverage for scanning beams. A key example is the Low-Frequency Array (LOFAR), developed by the Netherlands Institute for Radio Astronomy (ASTRON). LOFAR pioneered sparse array design in its Low-Band Antenna (LBA) system, which operates in the 10–80 MHz range. The LOFAR-LBA array uses a randomly exponential distribution layout strategy[12]. This enables large-scale array deployment, effectively reduces side lobe levels, and optimizes radiation pattern characteristics. Fig. 1A shows the sparse array topology of the LBA antenna layout. This design offers a valuable engineering reference for later radio astronomy array optimizations.

Building upon earlier efforts, in the subsequent development of the Long Wavelength Array (LWA), researchers, including Leonid Kogan and Aaron Cohen, employed an array configuration optimization algorithm designed to minimize side lobes, enhancing the antenna layout of the LWA-1 elliptical array[13] as shown in Fig. 1B and Fig. 1C.

In the proposed designs for subsequent arrays, such as the Square Kilometer Array (SKA), both sparse and dense configurations have been considered in optimizing the array layout. Specifically, random distribution strategies were employed to enhance the geometric configuration in the sparse configuration scenario[14–16].

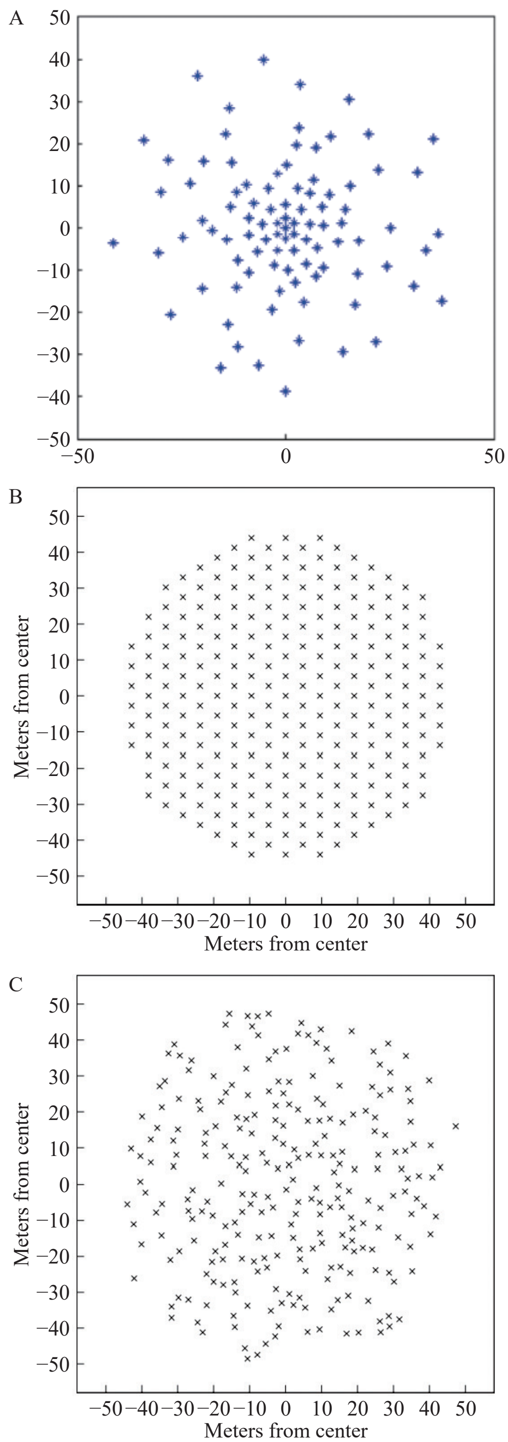

Fig. 1. Distribution map of typical sparse array formations. (A) Sparse distribution diagram of 96 LBA antennas for LOFAR. (B) Original regular array layout of LWA-1. (C) Sparse layout of LWA-1 after optimization.

In recent years, numerous studies have been conducted on the sparse layout optimization of radio antenna arrays. Di et al.[9] investigated the performance variation characteristics of radio antenna arrays under different scanning angles in wide-angle scanning scenarios and subsequently performed sparse layout optimization accordingly. Battaglia et al.[17] addressed the pattern synthesis requirements for the SKA in the low-frequency band (50–350 MHz), employing a convex programming approach to optimize the sparse array configuration while satisfying geometric constraints, effectively suppressing sidelobe levels. The proposed method was validated through full-wave simulations. Dong et al.[1] focused on the 30–300 MHz VHF band, systematically analyzing the technical challenges associated with sparse array deployment in this frequency range. They proposed a structured technical framework comprising array element arrangement optimization followed by signal processing system construction, and developed a high-performance computing platform integrated with Field-Programmable Gate Array (FPGA)-based System on Programmable Chip (SOPC) architecture to enable real-time computation and distribution of weighting parameters. This work provides critical technical support for the development of large-scale VHF radio astronomical arrays.

The core objective of array layout optimization is to adjust the inter-element spacing of antenna arrays to meet specific radiation performance requirements. Typical goals include optimization of beamwidth, peak sidelobe level (PSLL), number of elements, and null placement. The aim is to derive an optimal configuration of element positions that satisfies these criteria. Among these parameters, PSLL has the most significant impact on the sensitivity performance of radio telescopes. PSLL is a nonlinear function of the element positions, and minimizing PSLL by optimizing element placement is a nonlinear optimization problem, which is inherently complex to solve. To address this challenge, extensive research has been conducted in the field of sparse array layout optimization. Swarm intelligence optimization algorithms, including Genetic Algorithms (GAs)[18,19], the Grey Wolf Optimizer (GWO)[20,21], Particle Swarm Optimization (PSO)[22,23], and Differential Evolution (DE)[24], have been successfully applied.

Among various intelligent optimization algorithms, the GA[25] is a heuristic search method inspired by natural evolutionary processes in biological systems. Its design is based on Darwin's theory of natural selection and genetic principles. As a powerful optimization tool, GA is renowned for efficiency, practicality, and robustness. These qualities make it well-suited for solving complex, nonlinear, multimodal, and multi-objective optimization problems. The theoretical foundation and application of GA in array layout optimization have provided an effective approach for designing sparse antenna arrays. In 1994, Haunt et al.[26] were the first to apply GAs to the sparse array domain. They optimized a uniformly excited 200-element linear array and successfully reduced the PSLL to −20 dB. Recently, Sun et al.[27] conducted optimization simulations on several types of single-frequency linear arrays using a real-coded GA. They compared the performance of this algorithm with several improved GA versions under identical constraints. The results showed it consistently achieved lower PSLL values than the alternatives. Qin et al.[28] proposed an improved GA based on a penalty function mechanism. This controlled the sparsity rate and suppressed grating lobes by reducing the number of elements. Simulation results, under single-frequency conditions, demonstrated that the proposed GA-based sparse array improved the PSLL by 1.07–1.37 dB over existing methods.

Our work differs from the traditional planar array sparse distribution optimization and considers optimization under wide bandwidth conditions. We investigate sparse optimization of a 64-element planar radio antenna array operating in the 10–90 MHz frequency band using a GA based on real number coding. In contrast with traditional sparse array optimization design, we focus on analyzing optimization performance across various frequency points and scanning angles under high-bandwidth conditions. Key performance parameters of the sparse array, such as PSLL, gain, effective aperture, and sensitivity, are systematically analyzed. The GA iteratively derives the optimal element arrangement by minimizing the maximum PSLL across the entire frequency band. A comparative analysis between the optimized sparse array and a regular array, both with the same number of elements and bandwidth, shows a significant reduction in PSLL across the full frequency range for the sparse array. Sensitivity is also improved at all frequency points. Statistical analysis of grating lobe characteristics across various frequencies and scan angles shows that the sparse array shows markedly superior grating lobe suppression compared with the regular array. These results confirm the effectiveness and superiority of GA sparse distribution optimization in improving the performance of radio antenna arrays under wide bandwidth conditions.

2. THEORETICAL MODEL OF PLANAR RADIO ANTENNA ARRAYS

2.1. Radiation Pattern Synthesis Model for Planar Arrays

Within a planar array boundary of size $L \times H$, the antenna elements are regularly distributed. There are M array elements along the x-axis direction and N array elements along the y-axis direction. The total number of array elements, $Q = M \times N$. A diagram of the array element distribution is shown in Fig. 2.

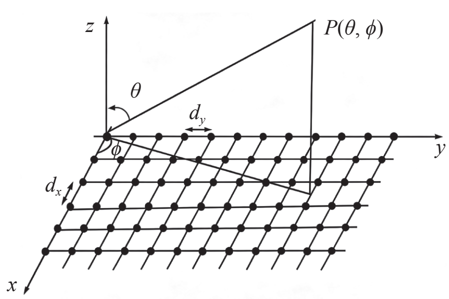

Fig. 2. Diagram of the two-dimensional planar distribution of a regular array.

In Fig. 2, d_x and d_y are the row spacing and column spacing of the array respectively. There exists a far field point $P(\theta,\phi)$, and the positions of all array elements fall within the planar array area. To meet the aperture design requirements of the array antenna, the position of the Q-th array element is fixed as the lower right corner vertex, (L,H), of the planar array. If the position of the Q-th array element is (x_m,y_n), then

$$\begin{cases} x_m = md_x & m = 0,1,2,\ldots,M-1 \\ y_n = nd_y & n = 0,1,2,\ldots,N-1 \end{cases}. \tag{2}$$

Based on the aforementioned element distribution and position constraints, the radiation pattern function of the planar array (assuming that all elements are ideal isotropic point sources, with no mutual coupling effects and uniform excitation amplitudes) can be expressed as the product of the element pattern $EP(\theta,\phi)$ and the array factor $AF(\theta,\phi)$, as given by

$$F(\theta,\phi) = EP(\theta,\phi)\cdot AF(\theta,\phi). \tag{3}$$

At this point, a signal incident on the array, from the direction (θ,ϕ), is received by each antenna element and coherently summed to form a synthesized signal. The coherently summed array factor, $AF(\theta,\phi)$, is expressed as shown as

$$\mathrm{AF}(\theta,\phi) = \sum_{m=1}^{M}\sum_{n=1}^{N} \mathrm{e}^{\mathrm{j}\left[\left(\frac{2\pi}{\lambda}x_m\sin\theta\cos\phi+\frac{2\pi}{\lambda}y_n\sin\theta\sin\phi\right)-\left(\frac{2\pi}{\lambda}x_m\sin\theta_0\cos\phi_0+\frac{2\pi}{\lambda}y_n\sin\theta_0\sin\phi_0\right)\right]}, \tag{4}$$

where $AF(\theta,\phi)$ is the array factor, λ is the wavelength (in meters), (θ,ϕ) gives the incident angles, and (θ_0,ϕ_0) is the beam scanning direction of the array.

In this study, we focus on the performance comparison of sparse array optimization, using a simplified model for analysis purposes. Individual differences among antenna elements are disregarded by assuming all elements are omnidirectional antennas. Thus, the element pattern remains constant and equal to 1 across the entire angular range[9]. Complex factors, such as mutual coupling between elements, are also omitted. With these simplifying assumptions, substituting Equation (4) into Equation (3) and carrying out the derivation leads to a simplified expression for the synthesized radiation pattern, shown as

$$F(\theta,\phi) = \sum_{m=1}^{M}\sum_{n=1}^{N} \mathrm{e}^{\mathrm{j}\left[\left(\frac{2\pi}{\lambda}x_m\sin\theta\cos\phi+\frac{2\pi}{\lambda}y_n\sin\theta\sin\phi\right)-\left(\frac{2\pi}{\lambda}x_m\sin\theta_0\cos\phi_0+\frac{2\pi}{\lambda}y_n\sin\theta_0\sin\phi_0\right)\right]}. \tag{5}$$

2.2. Sensitivity Evaluation Framework

In radio astronomical observations, sensitivity serves as a core metric for evaluating the performance of telescope, directly determining the receiving system's ability to detect weak celestial signals. Sensitivity is quantitatively determined by the minimum detectable radio source flux density, $S_{\min}$[7]. This parameter defines the minimum flux density in units of watts per square meter per hertz (W m^{-2} Hz^{-1}). A common astronomical unit of sensitivity is the Jansky (Jy), where 1 Jy = 10^{-26} W m^{-2} Hz^{-1}. A lower value of $S_{\min}$ indicates a stronger capability of the radio telescope to detect weak signals, signifying better sensitivity performance[9]. The calculation of sensitivity is given by

$$S_{\min} = \frac{kT_{\mathrm{sys}}}{A_{\mathrm{e}}\sqrt{tB}}, \tag{6}$$

where T_{sys} is the system temperature, B is the observation bandwidth, and t is the integration time. These three parameters are closely related to the antenna elements and the backend receiver. Because this study focuses on the impact of antenna array configuration on sensitivity, the term $T_{\mathrm{sys}}/\sqrt{tB}$ is treated as a constant C, A_{e} is the effective aperture area, and k is the Boltzmann constant. Together, these parameters play critical roles in both the derivation of the formula and the sensitivity analysis.

The effective aperture A_{e} can be calculated from the array gain, using the relation

$$A_{\mathrm{e}} = \frac{\lambda^2}{4\pi}G_0, \tag{7}$$

where λ is the wavelength, and G_0 is the array gain[9]. The gain G_0 is, in turn, calculated as

$$G_0 = \left(\frac{4\pi F^2(\theta,\phi)}{\int_0^{2\pi}\int_0^{\pi} F^2(\theta,\phi)\sin\theta\,\mathrm{d}\theta\,\mathrm{d}\phi}\right)_{\max}, \tag{8}$$

where $F(\theta,\phi)$ is the array radiation pattern function, as defined in Equation (5).

2.3. Simulation Benchmark Model for a Regular Array

We simulate a regular array, consisting of 64 elements arranged in an 8 × 8 grid, setting the operating bandwidth from 10–90 MHz, with an element spacing of $d = \lambda_{\min}/2$ (where $\lambda_{\min}$ is the wavelength at 90 MHz). The array aperture measures $3.5\lambda_{\min}\cdot 3.5\lambda_{\min}$, and the scanning angles are fixed at $\theta = 0°$, $\phi = 0°$ (see Fig. 3). The maximum PSLL ($PSLL_{\max}$) across the entire frequency band is −12.80 dB.

As shown in Fig. 3, the regular array is arranged with equal spacing. However, due to inherent constraints associated with fixed array apertures and the periodic distribution of element positions, such arrays are prone to generating PSLLs during the beamforming process. This limitation is not exclusive to rectangular regular arrays. Another configuration, the LWA hexagonal regular array discussed in Section 1, shows improved uniformity in field-of-view coverage, but similarly suffers from inadequate sidelobe suppression resulting from the periodic properties of isometric configurations. In the following sections, we will solve this problem by optimizing the array position.

3. SPARSE OPTIMIZATION OF PLANAR ARRAYS BASED ON GAS

3.1. GA Optimization Procedure and Parameter Design

For the sparse design process of planar antenna arrays using a GA, first, an initial population is generated, where each individual represents an initial array configuration, with a population size of NP[9]. The gene sequence of each individual is then sorted. In this study, the genes of an individual correspond to the inter-element spacings, and each individual represents a specific array element layout. The population thus represents a collection of these layout schemes.

Next, fitness values are calculated using a function tailored to the optimization goal, evaluating each array layout. Iterative adjustments follow: if the set number of generations is not reached, selection, crossover, and mutation are applied. Gene sequences are converted into actual

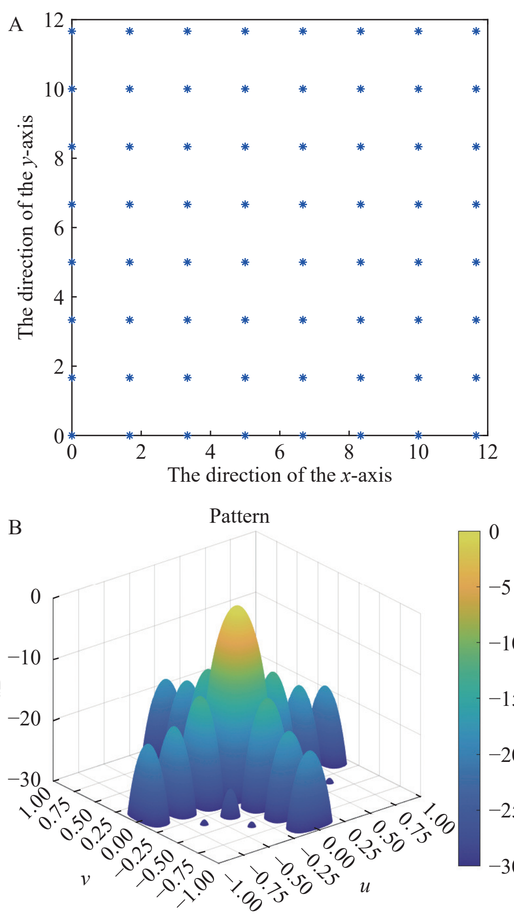

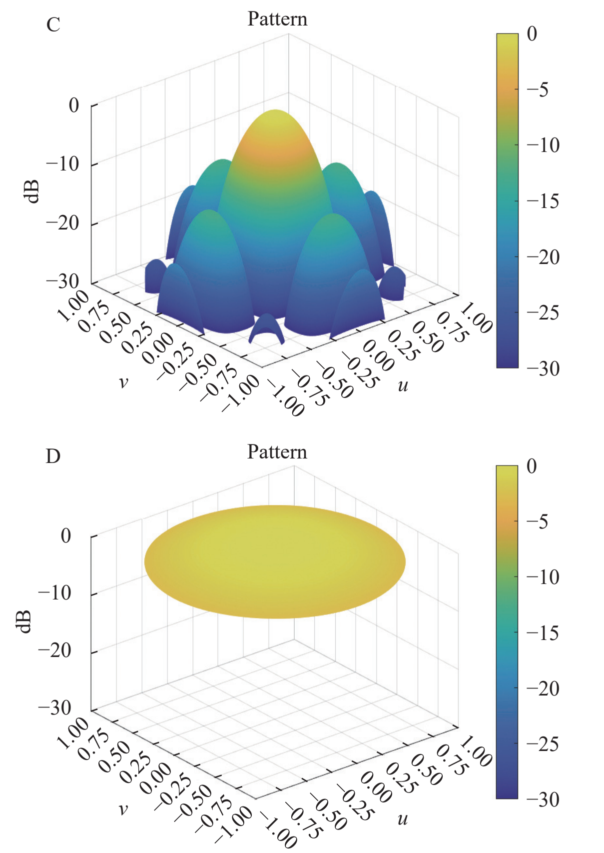

Fig. 3. Element distribution diagram and normalized radiation pattern of a regular array, with scanning angles of θ = 0° and ϕ = 0°. (A) Element distribution. (B) Radiation pattern at 90 MHz. (C) Radiation pattern at 50 MHz. (D) Radiation pattern at 10 MHz.

element positions, and fitness is recalculated. This cycle repeats until the generation limit is met. When the termination criterion is reached, the algorithm outputs the array configuration with the highest fitness. The overall procedure is shown in Fig. 4.

3.1.1. *Initialization of the initial population and array positions*

The initial population is generated based on a regular planar array with an aperture of $L \times H$. Here, L and H represent the array aperture lengths in the x- and y- directions, respectively. The number of antenna elements matches that of the regular array, and all elements are located on the x-y plane. The element positions are represented by a two-dimensional complex matrix $\boldsymbol{G}$, of size $M \times N$. Each matrix value corresponds to the position of an element, expressed as $dx + \mathrm{j}dy$. Here, dx_{mn} and dy_{mn} are the inter-element spacings in the x- and y- directions, respectively, for an element at position (m,n). This is given by the relation

$$\boldsymbol{G} = \begin{bmatrix} dx_{11} & dx_{12} & \cdots & dx_{1N} \\ dx_{21} & dx_{22} & \cdots & dx_{2N} \\ \vdots & \vdots & & \vdots \\ dx_{M1} & dx_{M2} & \cdots & dx_{MN} \end{bmatrix} +$$

$$\mathrm{j}*\begin{bmatrix} dy_{11} & dy_{12} & \cdots & dy_{1N} \\ dy_{21} & dy_{22} & \cdots & dy_{2N} \\ \vdots & \vdots & & \vdots \\ dy_{M1} & dy_{M2} & \cdots & dy_{MN} \end{bmatrix}. \tag{9}$$

Each gene, representing the inter-element spacing, must satisfy the spatial constraint conditions,

$$\begin{cases} s.t. 0 \leqslant dx_{mn} \leqslant L, 0 \leqslant dy_{mn} \leqslant H \\ |dx_{mn} - dx_{lk}| \geqslant d_c \\ |dy_{mn} - dy_{lk}| \geqslant d_c \\ m,n,l,k \in \mathbf{Z}, 1 \leqslant l,m \leqslant M, 1 \leqslant k,n \leqslant N \end{cases}, \tag{10}$$

where d_c is the minimum inter-element spacing constraint. Based on the above constraint conditions, the spacing dx_{mn} is decomposed into two parts, $x_{mn} + (m-1)d_c$, and similarly, dy_{mn} is expressed as $y_{mn} + (n-1)d_c$. By sorting the spacing values in each row and column in ascending order, we obtain the expressions,

$$\boldsymbol{dx} = \begin{bmatrix} x_{11} & x_{12} & \cdots & x_{1N} \\ x_{21} & x_{22} & \cdots & x_{2N} \\ \vdots & \vdots & & \vdots \\ x_{M1} & x_{M2} & \cdots & x_{MN} \end{bmatrix} +$$

$$\begin{bmatrix} 0 & 0 & \cdots & 0 \\ d_c & d_c & \cdots & d_c \\ \vdots & \vdots & & \vdots \\ (M-1)d_c & (M-1)d_c & \cdots & (M-1)d_c \end{bmatrix} \tag{11}$$

and

$$\boldsymbol{dy} = \begin{bmatrix} y_{11} & y_{12} & \cdots & y_{1N} \\ y_{21} & y_{22} & \cdots & y_{2N} \\ \vdots & \vdots & & \vdots \\ y_{M1} & y_{M2} & \cdots & y_{MN} \end{bmatrix} +$$

$$\begin{bmatrix} 0 & d_c & \cdots & (N-1)d_c \\ 0 & d_c & \cdots & (N-1)d_c \\ \vdots & \vdots & & \vdots \\ 0 & d_c & \cdots & (N-1)d_c \end{bmatrix}. \tag{12}$$

This ensures that, after satisfying the minimum inter-element spacing constraint, the remaining available length in the x-direction is $L-(M-1)d_c$, and in the y-direction is $H-(N-1)d_c$. Consequently, the search space in the x-direction is reduced from $[0, L]$ to $[0, L-(M-1)d_c]$, and in the y-direction from $[0, H]$ to $[0, H-(N-1)d_c]$. Compared with the original array layout algorithm, this reduction in the search space makes it easier to find an optimal solution.

If constrained element position matrix is $\boldsymbol{f}$, and the constraint matrix is $\boldsymbol{C}$, where $f(m,n) = x_{mn} + \mathrm{j} * y_{mn}$ and $C(m,n) = (m-1)d_c + \mathrm{j} * (n-1)d_c$, then, the final element position matrix, $\boldsymbol{G}$, must be the sum of $\boldsymbol{f}$ and $\boldsymbol{C}$. Therefore, during genetic operations, it is only necessary to manipulate the intermediate individual matrix $\boldsymbol{f}$, which effectively reduces the search space and accelerates the optimization process.

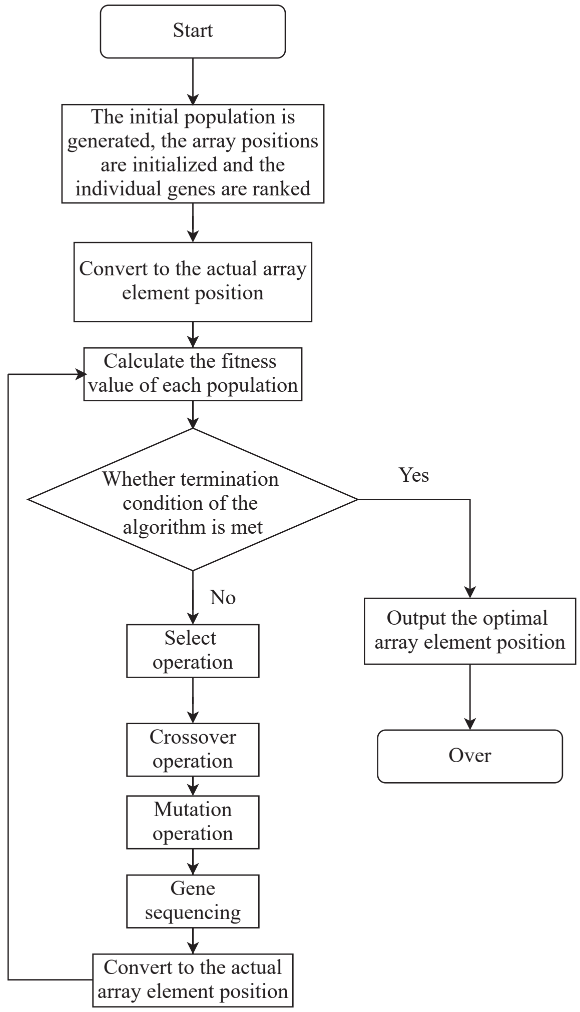

Fig. 4. Flowchart of sparse distribution optimization using a GA.

Additionally, since the array aperture is fixed, boundary constraints must also be applied to the array layout[9], as defined by

$$\begin{cases} dx_{11} = 0 \\ dx_{1N} = 0 \\ \cdots \\ dx_{M1} = L \\ dx_{MN} = L \end{cases} \tag{13}$$

and

$$\begin{cases} dy_{11} = 0 \\ dy_{1N} = 0 \\ \cdots \\ dy_{M1} = H \\ dy_{MN} = H \end{cases}. \tag{14}$$

This approach ensures that each of the four corners of the initialized array contains at least one element, thereby maintaining a constant array aperture throughout the subsequent optimization process.

During initialization, the array element positions of a regular array are used as the initial configuration. The population consists of NP individuals, with a number of generations, g. Each intermediate individual in the population is represented as

$$f_{ji} = x_{ji} + j \cdot y_{ji} (j = 1, 2, \cdots, M \times N, i = 1, 2, \cdots, NP), \quad (15)$$

where NP is the total number of individuals in a population, i is the index of an individual within that population, and j is the index of an antenna element within the individual.

3.1.2. *Fitness function*

For planar antenna array optimization, especially in the design of wideband arrays, it is essential not only to ensure that the radiation pattern at the upper operating frequency is free from grating lobes, but also to minimize the PSLL across the entire operating frequency band. Therefore, in this study, the fitness function is defined as the maximum value of the peak sidelobe level of the array radiation pattern in the 10–90 MHz frequency range, which can be expressed as

$$fit_i = PSLL_{\max}, \quad (16)$$

where fit_i is the fitness value of the i-th individual in the population, and $PSLL_{\max}$ is the maximum peak sidelobe level of the array radiation pattern within the 10–90 MHz frequency band. Different to other single-objective optimization problems, this is a multi-objective optimization problem, with the objective of minimizing the $PSLL_{\max}$ over the full 10–90 MHZ frequency band.

Since the PSLL value will indirectly affect the full frequency band gain, effective area and sensitivity, the optimization of this fitness function can also improve these three aspects (see Section 4.2).

3.1.3. *Selection, crossover, and mutation operations*

In this study, we use the roulette wheel selection method, wherein the probability of an individual being selected is proportional to its fitness value,

$$P_i = fit_i / \sum_{i=1}^{NP} fit_i. \quad (17)$$

This mechanism ensures that individuals with higher fitness values are more likely to be chosen, promoting the optimization of the algorithm. The selection operation is performed according to Equations (16) and (17). During the algorithm implementation, the PSLL at each frequency point within the 10–90 MHz band is obtained by identifying the highest value in the sidelobe region of the corresponding radiation pattern. By traversing all frequency points across the entire operating band, we can determine $PSLL_{\max}$.

To prevent the GA from premature convergence, crossover and mutation operations are applied to the selected individuals. The crossover rate and mutation rate are P_c and P_m, respectively. Instead of traditional binary-coded operations, real coded operations are used. In the crossover operation, each selected odd-indexed individual is paired with a corresponding even-indexed individual. For each pair, a portion of their genes, representing the inter-element spacing of the array, is exchanged with a probability of P_c. Specifically, for each odd-indexed gene, a random number is generated within the range [0, 1] and compared with the crossover probability, P_c. If the random number exceeds P_c, a random position in the gene sequence is selected, and the gene at this position in the odd-indexed individual is swapped entirely with a corresponding gene in a subsequent even-indexed individual. This process achieves gene recombination through positional exchange.

The mutation process is initiated based on a predefined mutation probability, P_m. The primary objective is to adjust the array spacing parameter by replacing certain genes within the chromosome. First, the intermediate population, generated after crossover, is sequentially evaluated, and for each individual, a random number, $\varepsilon \in [0, 1]$, is generated. This value is then compared with the mutation probability P_m. If $\varepsilon < P_m$, the individual is selected for mutation, and the gene, $g_{j,i}$, corresponding to the (j, i)-th array element is randomly chosen as the mutation target.

For the selected gene $g_{j,i}$, the parameter is updated using a random reset method, where the new gene value is computed using the relations,

$$x_{j,i} = \varepsilon \cdot [L - (M-1) d_{\min}] \quad (18)$$

and

$$y_{j,i} = \varepsilon \cdot [H - (N-1) d_{\min}], \quad (19)$$

where $d_{\min}$ is the minimum inter-element spacing constraint, while L and H are the dimensions of the planar array along the x-axis and y-axis, respectively. M and N are the numbers of array elements distributed along the x-axis and y-axis, respectively.

To ensure an orderly and reasonable element distribution, the inter-element spacing genes of all individuals in the new population are sorted in ascending order. As a result, we obtain the updated intermediate individual, $g'_{j,i}$, which satisfies the requirements for subsequent iterations.

Following the completion of selection, crossover, and mutation operations, the processed genetic information is reorganized to form a new population. Concurrently, the best individual from the previous generation is preserved and incorporated into the new population, to ensure that evolutionary progress consistently aligns with the optimization objective. By iteratively evaluating and comparing the fitness values according to Equation (16), and repeating the genetic operations until the predefined termination criterion is met, we achieve the optimal configuration for the planar sparse array antenna, resulting in the minimization of the sidelobe level in the radiation pattern.

3.2. Example of Sparse Optimization Using GA and Parameter Settings

A GA was applied to sparsely optimize the initial regular array. The operating bandwidth was set from 10–90 MHz, with 64 elements and an array aperture of $7\lambda_{\min}\cdot 7\lambda_{\min}$. The scanning angles were fixed at $\theta = 0°$, $\phi = 0°$. The population size was set to 50, the crossover rate to 0.8, the mutation rate to 0.08, and the number of generations to 100. The optimized array is shown in Fig. 5. $PSLL_{\max}$ over the entire frequency band was reduced to −13.84 dB.

The fitness evolution curves of the sparse optimization are shown in Fig. 5E, where black is the real-coded

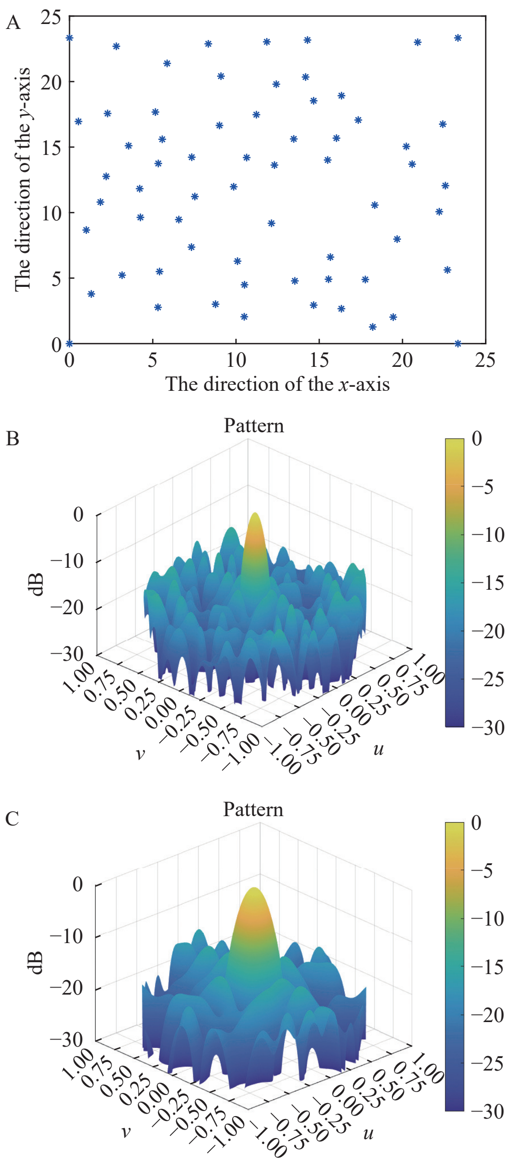

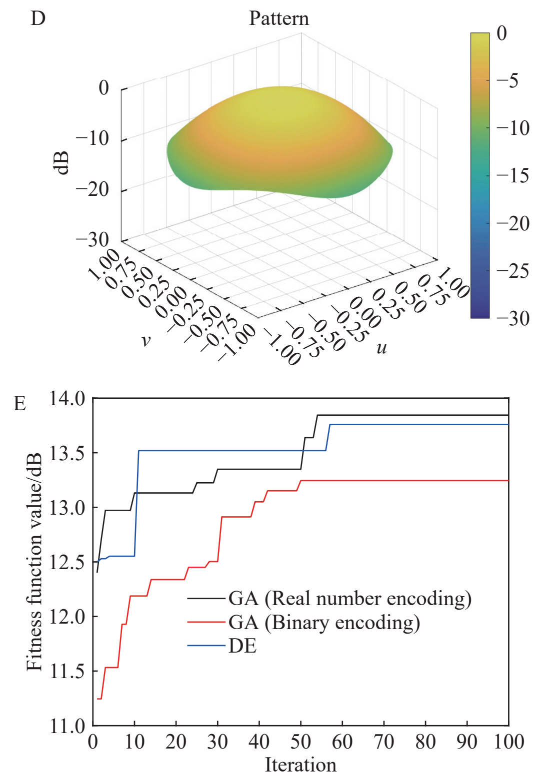

Fig. 5. Element distribution diagram and normalized radiation pattern of the sparse array, with scanning angles of $\theta = 0°$ and $\phi = 0°$. (A) Element distribution diagram. (B) Radiation pattern at 90 MHz. (C) Radiation pattern at 50 MHz. (D) Radiation pattern at 10 MHz. (E) Fitness evolution curves for the sparse optimization.

GA used in this paper, and red and blue are the binary real-coded GA and DE using the same fitness formula and related parameters. The fitness value of the proposed algorithm, after sparse distribution optimization, is significantly better than that of the most basic GA, and it is an improvement over the DE. For the evolution curve optimized by our algorithm, before the 54th generation, the fitness value continued to increase, and the optimal solution had not been found. After the 54th generation, the fitness value reached its optimum. This optimal array configuration was then retained for all subsequent generations until the 100th, when the GA terminated.

4. SIMULATION VALIDATION AND PERFORMANCE COMPARISON

Here, we evaluate the performance improvements from sparse optimization in radio antenna arrays, conducting a computational analysis of the radiation patterns of a 64-element planar antenna array optimized by a GA. We use a regular array with element spacing $d = \lambda/2$ as a reference model. This regular design theoretically prevents grating lobes and serves as a performance baseline. Through quantitative comparison of metrics like PSLL, sensitivity, and grating lobe suppression, we assess the effectiveness of sparse optimization in enhancing array performance.

4.1. Comparative Analysis of PSLL Suppression

Based on the simulated radiation pattern data for both the regular and sparse arrays, the PSLLs at selected frequency points within the operating band are compared in Table 1. A statistical analysis of the maximum PSLL across the bandwidth is conducted using Equation (16). The results indicate that within the 10–90 MHz operating band, the maximum PSLL of the 64-element planar regular array is −12.80 dB, whereas after GA-based sparse optimization, the $PSLL_{max}$ decreases to −13.84 dB, giving a reduction of 1.04 dB compared with the regular array.

Table 1. PSLLs of regular arrays and sparse arrays

Frequency/MHz	Regular array/dB	Sparse array/dB
36	−12.80	−13.84
42	−12.80	−13.84
48	−12.80	−13.84
54	−12.80	−13.84
60	−12.80	−13.84
66	−12.80	−13.84
72	−12.80	−13.84
78	−12.80	−13.86
84	−12.80	−13.85
90	−12.80	−13.84

4.2. Comparative Analysis of Observation Performance Parameters

Although the defined fitness function is only numerically related to PSLL, its value also indirectly affects G_0, A_e and S_{min}.

When PSLL decreases, the amplitude of far-area interference signals (such as strong source radiation or ground noise) received by the array decreases, and the system equivalent noise temperature, T_{sys}, decreases accordingly. According to Equation (6), when the effective area, A_e, observation time, T, and other parameters are unchanged, the reduction of T_{sys} will directly reduce the minimum detectable flow rate, S_{min}, i.e., the sensitivity will be improved.

The optimized sparse array can reduce PSLL and avoid the effective area loss caused by excessively sparse array elements, Using Equation (7), the array gain, G_0, increases as PSLL decreases and the beam energy is concentrated. This in turn increases A_e, and finally the sensitivity, S_{min}, is inversely increased according to Equation (6).

Therefore, this section proves the correctness of the sparse layout optimization mentioned in this paper from the three aspects of full-band gain, effective area improvement, and sensitivity improvement.

4.2.1. *Full-band gain characteristics analysis*

The gain was calculated using Equation (8). Table 2 lists the gain values at 10 MHz intervals.

From the simulation results of the array gain, within the 10–90 MHz bandwidth, the 64-element planar antenna array optimized through sparse configuration demonstrates a significant gain improvement compared with the regular array. Specifically, the regular array shows notable gain fluctuations across this frequency range, whereas the sparse array, by optimizing element layout, effectively suppresses gain variations caused by mutual coupling and spatial interference among elements. Such an improvement in gain performance not only enhances the antenna array's ability to receive weak radio signals but also substantially improves its observational stability in the complex electromagnetic environment of the HF-VHF band. This validates the effectiveness of the sparse optimization strategy in enhancing the overall performance of antenna arrays and adapting to the demands of astronomical observations within the HF-VHF frequency range.

Table 2. Comparison of gain between regular arrays and sparse arrays

Frequency/MHz	Regular array /dB	Sparse array /dB	Percentage increase
10	1.8	5.4	200%
20	6.8	11.7	72%
30	10.6	14.9	41%
40	12.7	17.0	34%
50	14.9	17.5	17%
60	16.2	18.6	15%
70	17.7	19.0	7%
80	18.6	19.7	6%
90	19.7	19.7	0%

4.2.2. *Comparative analysis of effective aperture enhancement*

Following the gain comparison between the sparse and regular arrays, we further investigate the performance of the antenna arrays by calculating the effective aperture based on Equation (7). The effective aperture data, obtained at 10 MHz frequency intervals, are detailed in Table 3. These data provide crucial support for an in-depth analysis of the impact of sparse optimization on the effective aperture of the antenna array, facilitating an evaluation of its contribution to the overall observational performance.

The effective aperture of the sparse array remains higher than that of the regular array across the entire bandwidth. Overall, the effective aperture decreases as the frequency increases, converging to the same value as the regular array at 90 MHz. Since the effective aperture is a critical parameter affecting sensitivity, it plays a vital role in determining the array's overall sensitivity performance.

4.2.3. *Mechanism analysis of sensitivity improvement*

After obtaining the effective aperture data of the antenna arrays, we substituted these values into Equation (6), to calculate the sensitivity. Based on this calculation procedure, we conducted a systematic analysis on the sensitivity performance of both the regular and sparse

Table 3. Comparison of effective areas between regular arrays and sparse arrays

Frequency /MHz	Regular array /m²	Sparse array /m²	Percentage increase
10	109.3	247.6	127%
20	85.4	266.4	212%
30	91.5	245.9	169%
40	84.1	225.7	168%
50	88.8	161.3	82%
60	82.8	144.1	74%
70	86.4	115.4	34%
80	81.4	104.2	28%
90	83.3	82.7	0%

arrays across the 10–90 MHz bandwidth. Table 4 gives detailed sensitivity $S_{\min}$ values at 10 MHz intervals. Combining these data allows an accurate comparison of the capabilities of the antenna arrays in detecting weak signals before and after sparse optimization. This offers critical evidence for comprehensively assessing the observational performance enhancements of the sparse array and further validates the effectiveness of sparse optimization in improving antenna array sensitivity.

Table 4. Comparison of sensitivity between regular arrays and sparse arrays ($T_{sys}/\sqrt{tB}$ is a constant C)

Frequency /MHz	Regular array/Jy	Sparse array/Jy	Percentage increase
10	12.6*C	5.6*C	56%
20	16.2*C	5.2*C	68%
30	15.1*C	5.6*C	63%
40	16.4*C	6.1*C	63%
50	15.5*C	8.6*C	45%
60	16.7*C	9.6*C	43%
70	16.0*C	12.0*C	25%
80	17.0*C	13.3*C	22%
90	16.6*C	16.7*C	0%

The calculated data indicate that within the 10–90 MHz frequency band, the sparse array's sensitivity performance consistently surpasses that of the regular array, as evidenced by its lower minimum detectable radio source flux density ($S_{\min}$) values. This advantage is particularly pronounced in the low to mid-frequency range of 10–50 MHz: at 10 MHz, the sparse array's sensitivity improves by 56% compared with the regular array; at 50 MHz, the improvement remains substantial at 45%, and as the frequency increases towards 90 MHz, the sensitivity of the sparse array gradually decreases (with $S_{\min}$ values rising), ultimately converging to parity with the sensitivity of the regular array at 90 MHz. Comparison curves of the regular array and the sparse array in full frequency band gain, effective aperture, and sensitivity are shown in Fig. 6.

The sparse array shows unique frequency response characteristics in terms of full-band gain, effective area, and sensitivity when considering the requirements of wideband operation and grating lobe suppression. This provides an important reference for the subsequent optimization design of radio antenna arrays.

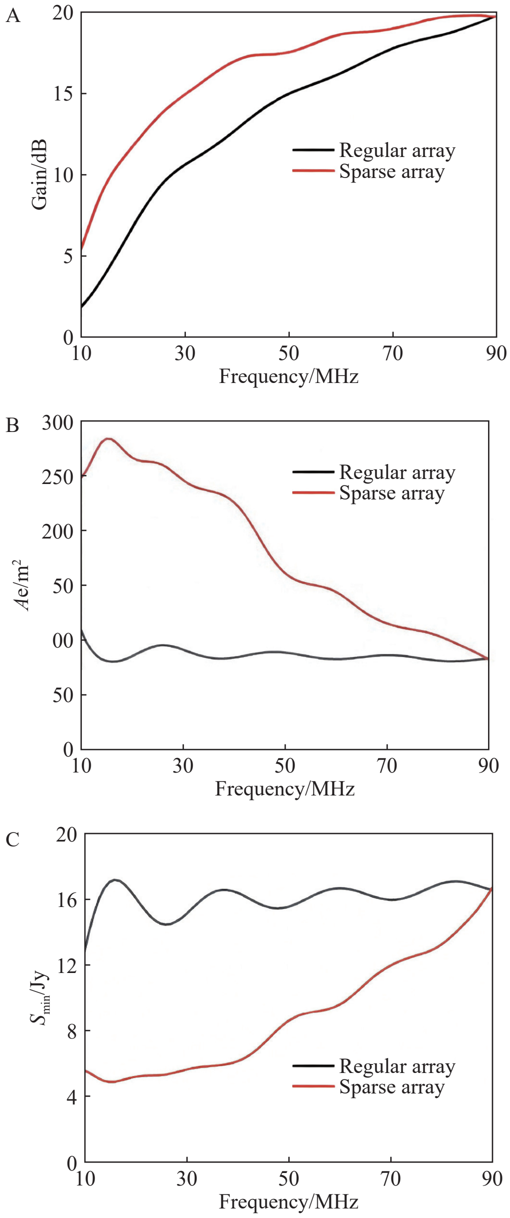

Fig. 6. Comparison of regular arrays and sparse arrays. (A) Gain comparison curves of regular arrays and sparse arrays. (B) Comparison curve of the effective areas between regular arrays and sparse arrays. (C) Sensitivity comparison curves of regular arrays and sparse arrays.

4.3. Wideband Grating Lobe Suppression Performance Verification

Sparse arrays shows excellent grating lobe suppression. To validate this in a wideband context, we conducted a comparative analysis, comparing a sparse array against a regular array with the same aperture size and number of elements (aperture of $7\lambda_{\min}\cdot 7\lambda_{\min}$ and 64 elements). Using Equation (1), we calculated the scan angle, θ, for grating lobe occurrence at operational frequencies for the regular array, then evaluated the sparse array's radiation pattern at these angles to assess suppression. Our analysis focused on three frequency points, 50 MHz, 60 MHz, and 70 MHz, using these to verify the effectiveness of grating lobe suppression.

To further validate the grating lobe suppression capability of the sparse array, Fig. 7 shows the normalized radiation patterns at 50 MHz across a scanning angle, θ, ranging from 10° to 60°. Based on results derived from Equation (1), the regular array generates a distinct grating lobe when the scan angle reaches θ = 53°, as evident in its radiation pattern at this angle. In contrast, the sparse array, optimized through a GA, shows no grating lobe under identical scanning conditions. This confirms that optimized element placement in the sparse array suppresses grating lobe interference associated with scan angle variations. The sparse array maintains main beam integrity and lowers sidelobe levels, offering a robust solution for wide-angle scanning observations.

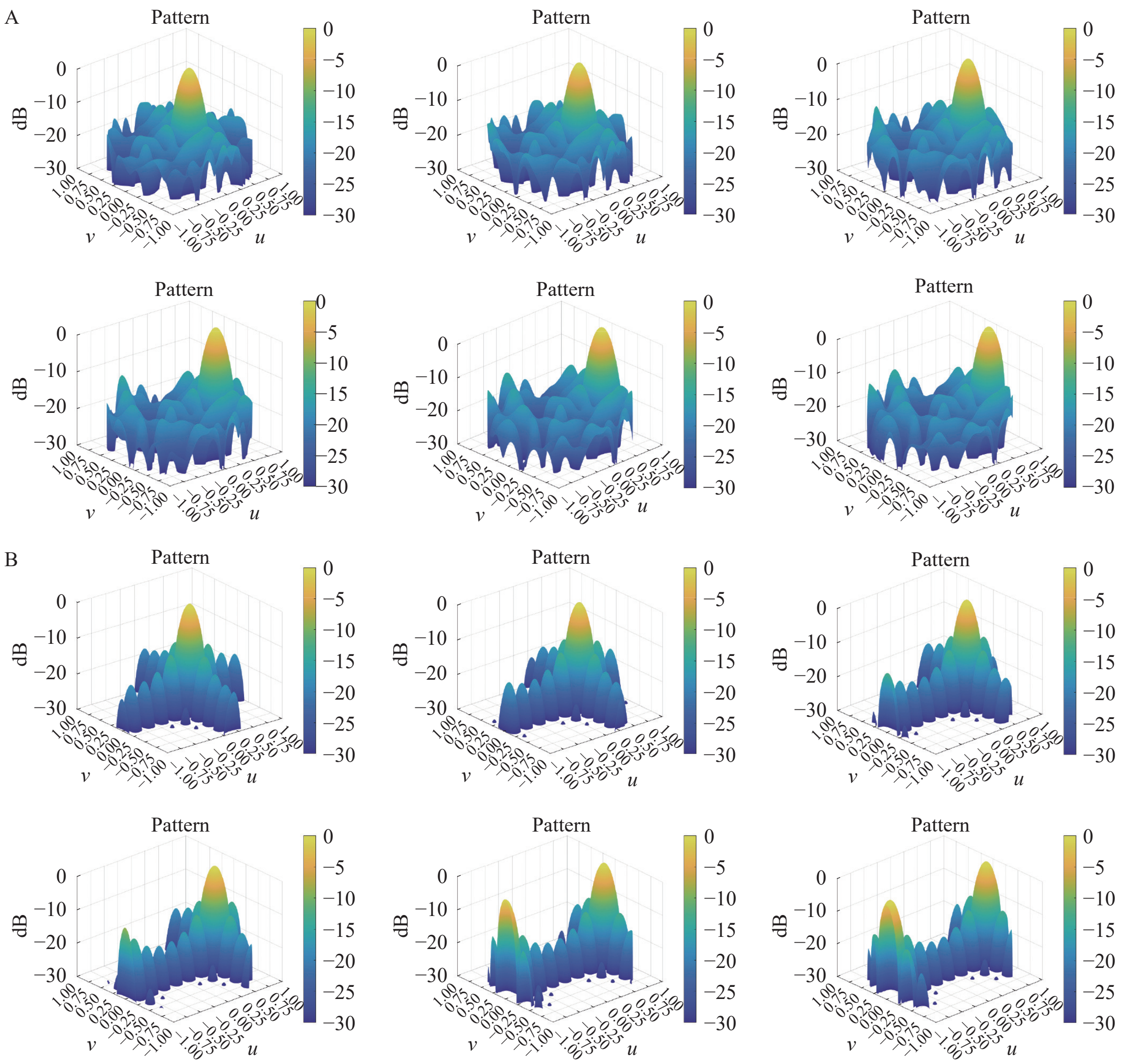

Fig. 7. Normalized radiation patterns at 50 MHz at different scanning angles, θ, of 10°, 20°, 30°, 40°, 53°, and 60° from left to right. (A) PSLL variation for a sparse array. (B) PSLL variation for a regular array.

Fig. 8 shows the normalized radiation patterns at 60 MHz for scan angles, θ, ranging from 10° to 60°. According to calculations based on Equation (1), the regular array begins to show grating lobes when the scan angle increases to θ = 30°, as seen in the radiation pattern of the regular array at this angle, where a pronounced grating lobe appears. In contrast, the sparse array does not show any grating lobes under the same scanning condition.

Fig. 9 shows normalized radiation patterns at 70 MHz for scan angles, θ, ranging from 10° to 60°. Based on calculations using Equation (1), the regular array shows grating lobes when the scan angle increases to θ = 15°, evident from the radiation pattern of the regular array at θ = 15°, where a significant grating lobe appears. By contrast, the sparse array, under the same scanning condition, shows no signs of grating lobes, highlighting its effectiveness in suppressing grating lobe formation at higher frequencies and tighter scan angles. Table 5 shows PSLL

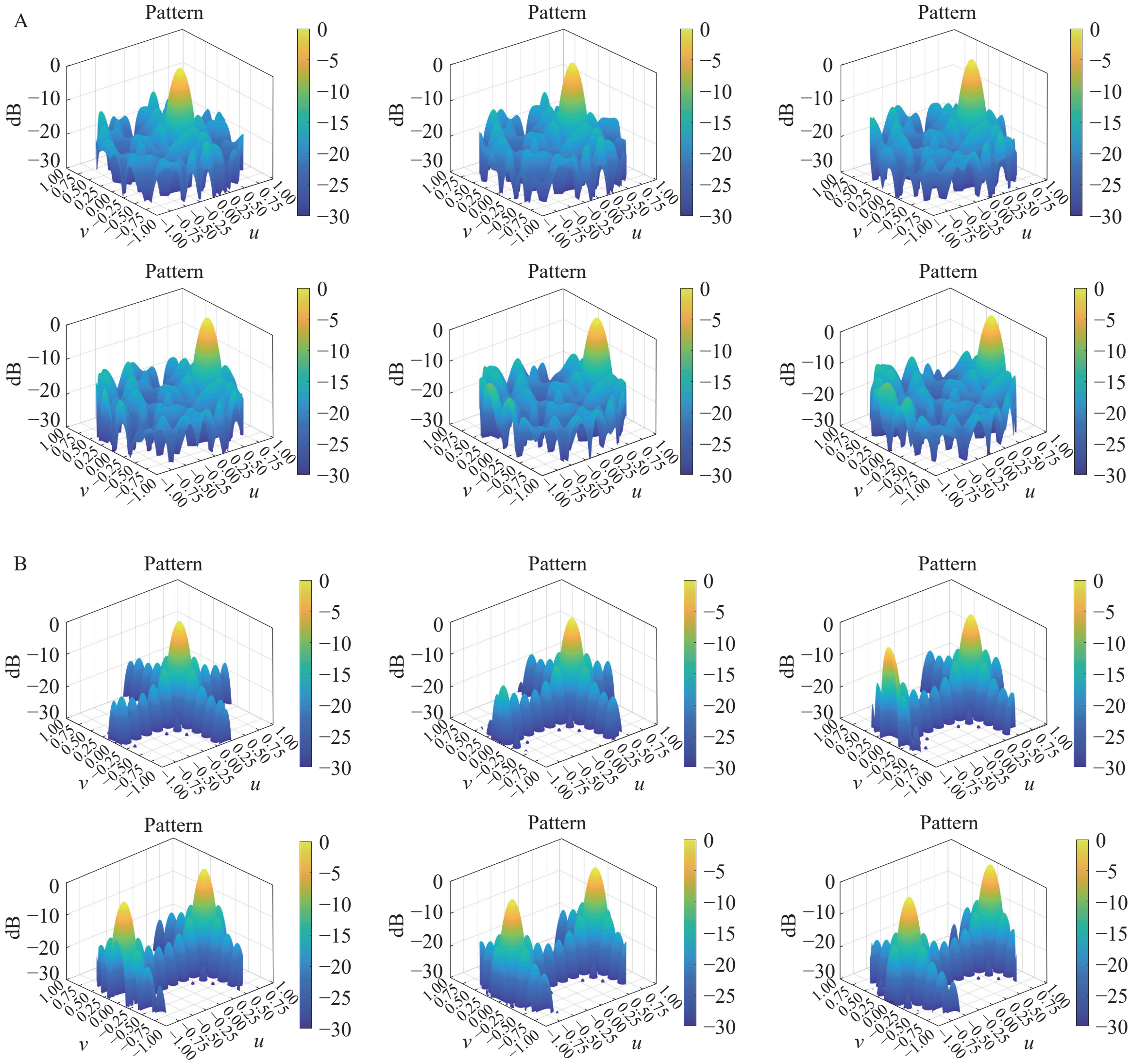

Fig. 8. Normalized radiation patterns at 60 MHz at different scanning angles, θ, of 10°, 20°, 30°, 40°, 50°, and 60° from left to right. (A) PSLL variation for a sparse array. (B) PSLL variation for a regular array.

variations for regular and sparse arrays at each scanning angle at 50, 60 and 70 MHz.

From the perspective of scan angle variation, the regular array shows significant grating lobe phenomena follow-

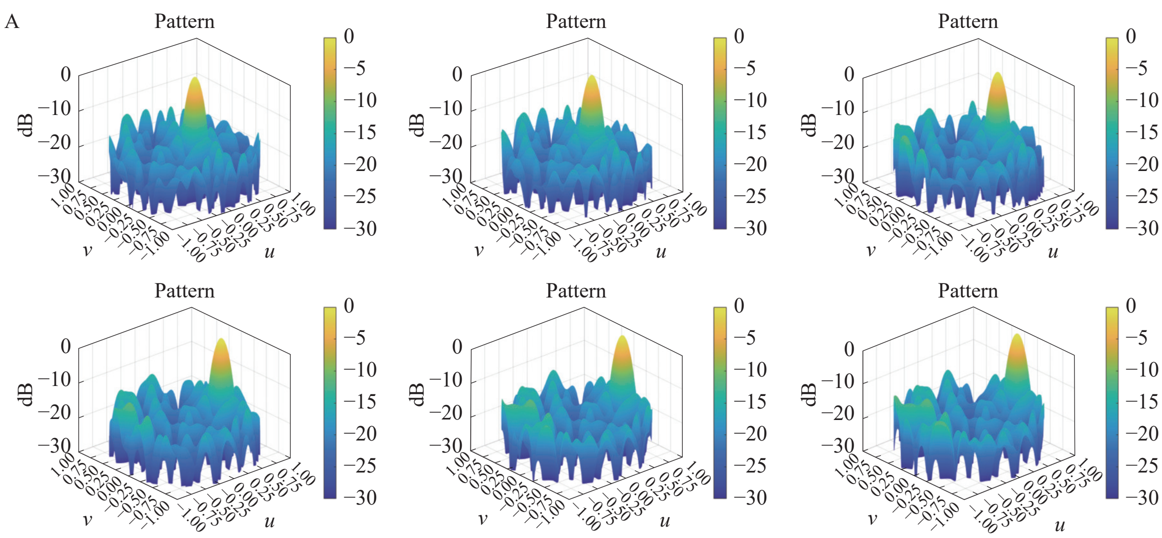

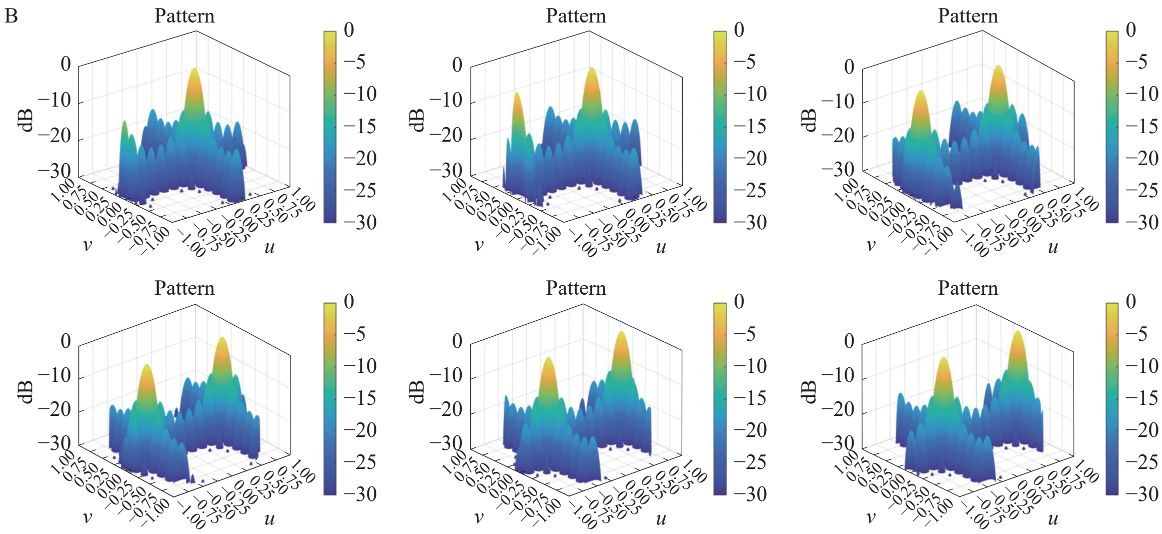

Fig. 9. Normalized radiation patterns at 70 MHz at different scanning angles, θ, of 10°, 15°, 30°, 40°, 53°, and 60° from left to right. (A) PSLL variation for a sparse array. (B) PSLL variation for a regular array.

ing scan adjustments. Under the ideal assumption that the element radiation pattern maintains a constant value of 1 across all angles, the grating lobe intensity can become comparable to that of the main lobe, severely interfering with effective signal reception and accurate target localization. By contrast, the GA-optimized sparse array consistently avoids the appearance of grating lobes within the same range of scan angle variation, directly demonstrating the superior grating lobe suppression capability of the sparse array.

Owing to the strategically optimized element distribution, the sparse array effectively mitigates grating lobe interference and substantially broadens the observable scanning region. Compared with a regular array, it shows greater adaptability and improved observational performance in complex scanning scenarios, thereby offering a more robust technical solution for wide-angle, multi-directional observations in radio astronomy.

Table 5. Comparison of PSLLs between regular and sparse arrays at different scanning angles, at 50, 60, and 70 MHz

Scanning angle θ/(°) at 50 MHz	The PSLL of the regular array/dB	The PSLL of the sparse array/dB	Scanning angle θ/(°) at 60 MHz	The PSLL of the regular array/dB	The PSLL of the sparse array/dB	Scanning angle θ/(°) at 70 MHz	The PSLL of the sparse array/dB	The PSLL of the sparse array/dB
10	−12.80	−13.84	10	−12.81	−13.84	10	−8.49	−13.84
20	−12.80	−13.84	20	−12.80	−13.85	15	−13.84	−13.84
30	−12.80	−13.84	30	0	−13.84	30	0	−11.32
40	−8.54	−13.84	40	0	−13.78	40	0	−10.60
53	−0.32	−13.84	50	0	−11.32	50	0	−7.51
60	0	−13.84	60	0	−11.31	60	0	−7.50

5. CONCLUSIONS

In radio astronomy within the HF-VHF frequency range, performance optimization of planar antenna arrays is essential for enhancing observational quality. Departing from conventional sparse array optimization approaches, focused on single frequency points, this study targets the critical HF-VHF astronomical band and adopts a broadband optimization strategy. The primary objective is to minimize the maximum PSLL across the entire frequency band. A GA is employed to perform sparse optimization of the wideband radio antenna array, resulting in an optimal element distribution scheme.

We have conducted an empirical study on a 64-element planar radio antenna array operating within the 10–90 MHz frequency range. Simulation results show that the sparse array shows notable performance advantages. For PSLL, the normalized radiation pattern of the sparse array achieves a PSLL reduction from −12.80 dB, as seen in the regular array, to −13.84 dB, giving a 1.04 dB improvement. In terms of sensitivity, the sparse array outperforms the regular array across all frequency points. The minimum detectable flux density, $S_{\min}$, generally increases with frequency, indicating a sensitivity decline. However, the sparse array shows a marked advantage in the low-frequency range. Sensitivity improves by 56% at 10 MHz and by 45% at 50 MHz. At 90 MHz, the sparse and regular arrays have equal sensitivity. Directional scanning tests were performed at three representative frequencies of 50 MHz, 60 MHz, and 70 MHz, conducted at varying scan angles. These tests confirm the superiority of the sparse array in sidelobe suppression. When the scan angle, θ, reaches 53° at 50 MHz, 30° at 60 MHz, and 15°

at 70 MHz, the regular array shows pronounced grating lobes, while the sparse array consistently maintains excellent grating lobe suppression.

These findings demonstrate that the GA-optimized sparse antenna array outperforms the conventional regular array with a lower PSLL, higher sensitivity, and a significantly broader observable scanning range. These improvements provide a more advanced technical solution for astronomical observations in the HF-VHF frequency band, offering important implications for enhancing observational capabilities at these critical frequencies. Future work will explore the application of more advanced algorithms, address practical deployment challenges such as mutual coupling among sensors, and extend the scope to more comprehensive objective optimization problems.

ACKNOWLEDGEMENTS

This work was supported by the Special Project for Building a Science and Technology Innovation Center Facing South and Southeast Asia–Yunnan Provincial International Joint Innovation Platform: the SKA Special Project of the Ministry of Science and Technology of the People's Republic of China (2020SKA0110202); "Yunnan Provincial China-Malaysia International Joint Laboratory of Advanced Radio Astronomy Technology at HF-VHF Bands" (202303AP140003); the Cultivation Project of Joint Fund for Astronomy under the National Natural Science Foundation of China (U2031133); the International Partnership Program of the Bureau of International Cooperation, Chinese Academy of Sciences: "Belt and Road" Cooperation (114A11KYSB20200001); the Kunming Municipal Foreign (International) Cooperation Base Project: "Joint R&D Cooperation Base for Advanced Radio Astronomy Technology between Yunnan Observatories, Chinese Academy of Sciences and University of Malaya" (GHJD-2021022); the Key Special Project "Intergovernmental International Science and Technology Innovation Cooperation" under the National Key R&D Program of the Ministry of Science and Technology of the People's Republic of China: "China-Malaysia Cooperative Research on Space Remote Sensing and Radio Astronomy Observation of Space Weather at Mid-Low Latitudes" (2022YFE0140000), and the SKA Special Project of the Ministry of Science and Technology of the People's Republic of China—High-Precision Calibration Method for Low-Frequency Radio Interferometric Arrays (2020SKA0110300). The Technology "Compact Team" Talent Project of Urumqi "Hongshan Science Innovation Talent" Cluster Program (B241018006). We are grateful to Yunnan Observatories, Chinese Academy of Sciences, for its support.

AI DISCLOSURE STATEMENT

AI-assisted technology is not used in the preparation of this work.

AUTHOR CONTRIBUTIONS

Yifeng Qin provided research and development ideas, conducted some experiment simulations, participated in paper review and editing, and drafted the manuscript. Jiarui Di contributed experimental concepts, operational steps, and performed some simulations. Liang Dong guided experiments and assisted in writing. Lesheng He, Zamri Zainal Abidin, Huanhuan Xie, and Wei He contributed to the hardware considerations in the design, providing practical parameters and identifying key issues that need to be taken into account. Yan Liu, Tarik Abdul Latef, Mohamadariff Othman, and Ning Zhang are responsible for recording the experimental data. All authors read and approved the final manuscript.

DECLARATION OF INTERESTS

The authors declare no competing interests.

REFERENCES

[1] Dong, L., Zhang, M., Xie, H. H., et al. 2023. The key technology analyses and researches of the sparse array in VHF band in radio astronomy. *Astronomical Research and Technology*, **20**(5): 421437.

[2] Morosan, D. E., Gallagher, P. T., Zucca, P., et al. 2014. LOFAR tied-array imaging of Type III solar radio bursts. *Astronomy and Astrophysics*, **568**: A67.

[3] Yan, Y. H. 2021. Research advances in solar physics at National Astronomical Observatories of Chinese Academy of Sciences. *Chinese Science Bulletin*, **66**(11): 1363−1384.

[4] Ping, J. S., Wang, M. Y., Zhang, M., et al. 2021. Introduction of space exploration progress for planetary radio burst emission. *Journal of Deep Space Exploration*, **8**(1): 80−91. (in Chinese)

[5] Caleb, M., Lenc, E., Kaplan, D. L., et al. 2024. An emission-state-switching radio transient with a 54-minute period. *Nature Astronomy*, **8**: 1159−1168.

[6] Deboer, D. R., Papsons, A. R., Aguirre, J, E., et al. 2015. Hydrogen epoch of reionization array (HERA). In Proceedings of the 2015 USNC-URSI Radio Science Meeting.

[7] Wu, Y., Du, B., Jin, C. J., et al. 2016. Review of new antenna technologies for the square kilometre array. *Chinese Journal of Radio Science*, **31**(2): 413−419. (in Chinese)

[8] Mailloux, R. J. 2005. Phased array antenna handbook. Boston: Artech House.

[9] Di, J. R., Dong, L., He, W. 2025. Sparse optimization of planar radio antenna arrays using a genetic algorithm. *Astronomical Techniques and Instruments*, **2**(2): 100−110.

[10] Rolfs, G. N. I. 2008. Tools of radio astronomy. Beijing: Beijing Normal University Press. (in Chinese)

[11] Rocca, P. G., Oliveri, R. J., Mailloux and Massa, A. 2016. Unconventional Phased Array Architectures and Design Methodologies—A Review. In Proceedings of the IEEE.

[12] Nijboer, R. J., Pandey-Pommier, M., Bruy, A. G. 2009. SKA Memo 113# LOFAR imaging capabilities and system sensitivity.

[13] Kogan, L., Cohen, L. 2005. LWA Memo #21 Elliptical

LWA station configurations optimized to minimize side lobes.

[14] de Vaate, J. G. B., Davidson, D. B., Razavi-Ghods, N. 2017. Sparse-regular aperture array SKA telescope concept. In Proceedings of Progress In Electromagnetics Research Symposium-Spring(PIERS).

[15] de Lera Acedo, E., Bolli, P., Paonessa, F., et al. 2018. SKA aperture array verification system: electromagnetic modeling and beam pattern measurements using a micro UAV. *Experimental Astronomy*, **45**: 1−20.

[16] Dewdney, P., Wagg, J., Braun, R., et al. 2016. SKA1-Low configuration-constraints & performance analysis. SKA Office, available from https://www.skao.int/sites/default/files/documents/d17-SKA-TEL-SKO-0000557_01_-DesignConstraints-1.pdf.

[17] Battaglia, G. M., Caruso, G., Bolli, P., et al. 2025. Low-frequency square kilometer array pattern optimization via convex programming. *Applied Sciences*, **15**(11): 5929.

[18] He, J., Feng, D. Z., Meng, C., et al. 2015. L-shape sparse array optimization based on genetic algorithm in MIMO radar. *Telecommunication Engineering*, **55**(8): 872−878. (in Chinese)

[19] Zhang, X., Zhang, Q. L., Zhang, X. 2017. Nonuniform antenna array design by parallelizing three-parent crossover genetic algorithm. *EURASIP Journal on Wireless Communications and Networking*, **2017**: 106.

[20] Tao, K., Wang, B., Tian, X., et al. 2024. Sparse rectangular planar array antenna synthesis based on improved grey wolf optimizer algorithm and window function weighting. *Chinese Journal of Radio Science*, **39**(3): 492−501. (in Chinese)

[21] Yao, Q. H., Xiang, T. M., Sun, B. 2021. Antenna design optimization based on improved grey wolf algorithm. *Journal of Hangzhou Dianzi University (Natural Science Edition)*, **41**(1): 31−37. (in Chinese)

[22] Brahma, D., Deb, A. 2020. Optimal design of antenna array using tuned random drift particle swarm optimization algorithm. In Proceedings of 2020 IEEE International IOT, Electronics and Mechatronics Conference (IEMTRONICS).

[23] Jiang, W., Kuang, Y. L., Zhang, X. 2020. Large-scale array antenna sparse distribution based on particle swarm optimization algorithm and position error impact analysis. In Proceedings of 2022 International Conference on Microwave and Millimeter Wave Technology (ICMMT).

[24] Gao, T. Y., Jiao, Y. C., Zhang, X. Y., et al. 2024. A hybrid self-adaptive differential evolution algorithm with simplified Bayesian local optimizer for efficient design of antennas. *IEEE Transactions on Antennas and Propagation*, **73**(1): 391−404.

[25] Ares-Pena, F., Rodriguez Gonzalez, J., Villanueva-Lopez, E., et al. 1999. Genetic algorithms in the design and optimization of antenna array patterns. *IEEE Transactions on Antennas and Propagation*, **47**(3): 506−510.

[26] Haupt, R. L. 1994. Thinned arrays using genetic algorithms. *IEEE Transactions on Antennas and Propagation*, **42**(7): 993−999.

[27] Sun, J. B., Li, J. B., Wang, D., et al. 2022. Thinned array synthesis based on real-coded genetic algorithm. *Telecommunication Engineering*, **62**(9): 1272−1277. (in Chinese)

[28] Qin, M., Hao, C. H. 2021. Optimization design of sparse stereoscopic antenna array based on improved genetic algorithm. *Journal of Chongqing University of Technology (Natural Science)*, **35**(8): 170−176. (in Chinese)